JPhys Materials

OPEN ACCESS

RECEIVED
4 September 2019

REVISED
1 October 2019

ACCEPTED FOR PUBLICATION
23 October 2019

PUBLISHED
21 November 2019

PAPER

Mesoscopic valley filter in graphene Corbino disk containing a p–n junction

Dominik Suszalski, Grzegorz Rut and Adam Rycerz[1]

Marian Smoluchowski Institute of Physics, Jagiellonian University, Łojasiewicza 11, PL–30348 Krakow, Poland
[1] Author to whom any correspondence should be addressed.

E-mail: rycerz@th.if.uj.edu.pl

Keywords: valleytronics, graphene, quantum transport, quantum Hall effect

Abstract

The Corbino geometry allows one to investigate the propagation of electric current along a p–n interface in ballistic graphene in the absence of edge states appearing for the familiar Hall-bar geometry. Using the transfer matrix in the angular-momentum space we find that for sufficiently strong magnetic fields the current propagates only in one direction, determined by the magnetic field direction and the interface orientation, and the two valleys, K and K', are equally occupied. Spatially-anisotropic effective mass may suppress one of the valley currents, selected by the external electric field, transforming the system into a mesoscopic version of the valley filter. The filtering mechanism can be fully understood within the effective Dirac theory, without referring to atomic-scale effects which are significant in proposals operating on localized edge states.

1. Introduction

One-dimensional conduction channels associated with edge states are often considered as background for solid-state quantum information processing not only in systems showing the quantum Hall effect [1–8], but also in graphene [9, 10] or transition metal dichalcogenide nanoribbons [11]. The aforementioned nanostructures are formed of two-dimensional materials that host an additional electronic valley degree of freedom, allowing dynamic control and the development of valleytronic devices [12], such as the valley filter [13, 14].

The operation of early proposed valley filters in graphene, employing the constriction with zigzag edges [13] or the line defect [15], was strongly affected by atomic-scale defects [16] and local magnetic order [17]. To overcome these difficulties, alternative proposals utilizing strain-induced pseudomagnetic fields [18–23], disorder and curvature effects in carbon nanotubes [24], or various types of domain walls in graphene, bilayer graphene [25], or topological systems [26, 27], were put forward. Despite such theoretical and computational efforts the experimental breakthrough is still missing, although some recent progress can be noticed [28–30]. Therefore, conceptually novel mechanisms of valley filtering are very desired.

In this paper, we explore the possibility of valley filtering for peculiar edge states mixing Landau levels from both sides of the p–n interface in the quantum Hall regime [4–6]. Such unconventional edge states can be regarded as degenerate versions of snake states, recently observed in ultraclean graphene devices [31, 32] (see figure 1). As the charge density is centered far from physical edges of the system, and transport is essentially of a *mesoscopic*, rather than nanoscopic, nature (i.e. the wavefunction varies on a length scale given by the magnetic length $l_B = \sqrt{\hbar/eB} \gg a$, with $a = 0.246$ nm being the lattice parameter; see [33]), some of the above-mentioned obstacles in sustaining the valley polarization of current may be overcome. Additionally, the Corbino geometry [34–37] allows one to eliminate conventional edge states, making it possible to fully control the spatial distribution of electric current via external electric and magnetic fields.

Possible classical carrier trajectories for weak-to-moderate magnetic fields are depicted schematically in the top and middle panels of figure 1. Snake states (bottom panel) cannot be understood fully classically, as they involve relativistic Klein tunneling through the region of an opposite polarity. In the quantum Hall regime the current flows along one section of the p–n interface only (see figure 2). The physical meaning of a 'weak',

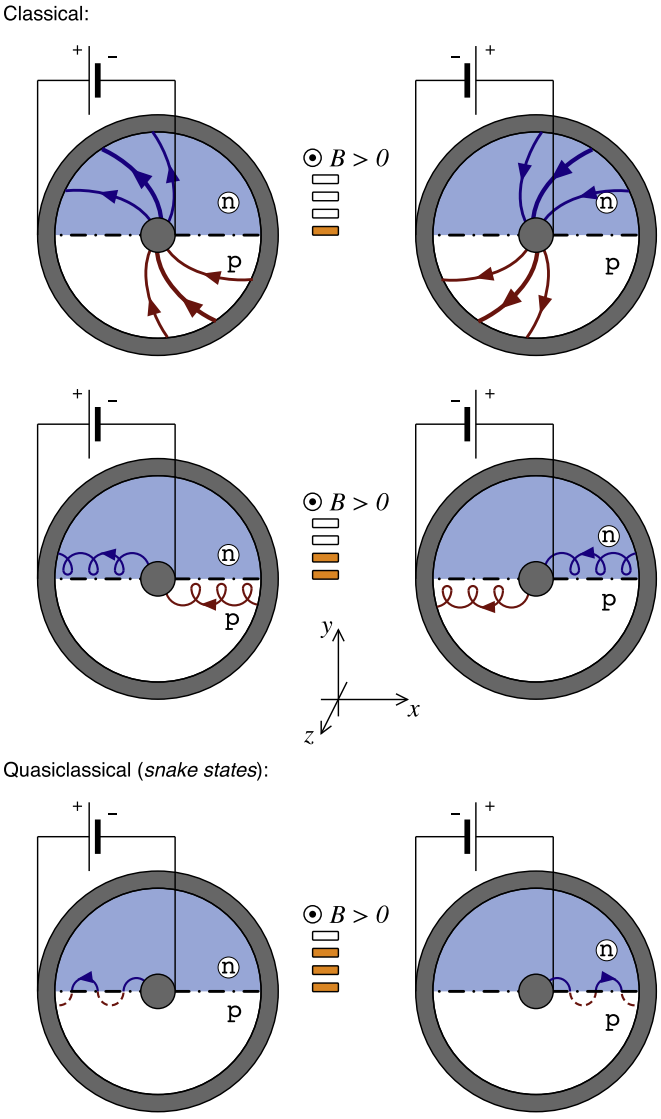

Figure 1. Classical and quasiclassical trajectories (schematic) for electrons (blue lines with arrows) and holes (red lines with arrows) in graphene Corbino disk containing a p–n junction (black dash-dot line) placed in a weak (top panel), moderate (middle panel), and strong (bottom panel) magnetic field $\boldsymbol{B} = (0,\ 0,\ B)$, with $B > 0$. Left and right subplots correspond to the opposite polarity of a voltage source driving a current between circular leads (shadow areas). The coordinate system used in the calculations is also shown.

'moderate', or 'strong', field is determined by mutual relations between the characteristic sample length $L \equiv R_o - R_i$ (with the outer disk radius R_o and the inner radius R_i), the magnetic length l_B ($\propto B^{-1/2}$), and the cyclotron radius r_c ($\propto B^{-1}$)[2]. In turn, the larger the disk size the lower field is required to eliminate currents distant from the p–n interface, providing the sake of scalability missing in previously proposed nanoscopic valley filters[3].

We show, using the numerical transfer-matrix technique, that the presence of a non-uniform staggered potential, introducing the position-dependent mass term in the effective Dirac equation for low-energy excitations [38], leads to a spatial separation of valley currents and that the valley polarization may be controlled by changing the gate potentials (see figure 3). Although to set a staggered potential one needs to initially modify the sample on a microscopic level, e.g. by chemical functionalization [39–41] or the adsorption of hexagonal boron nitride (h-BN) [42, 43], the operation of such a *mesoscopic valley filter* is then fully-electrostatically controlled. We further find, that the constant magnetic field of 1 T is sufficient to obtain a nearly perfect polarization in the disk of a 400 nm diameter. What is more, the filter operation can be directly attributed to a peculiar combination of symmetry breakings for the Dirac Hamiltonian: The mass term breaks the effective

[2] Related to the *local* carrier concentration via $r_c = \hbar k/eB = \sqrt{\pi|n|}\ l_B^2$, with $k = \sqrt{\pi|n|}$ being the wave vector.

[3] For $r_c \lesssim l_B$, quantum effects dominate and may fully eliminate the moderate-field range (see middle panel in figure 1) for smaller disks. As r_c is related to the carrier concentration, particular scenario of the classical-to-quantum transition also depends on the electrostatic potential profile.

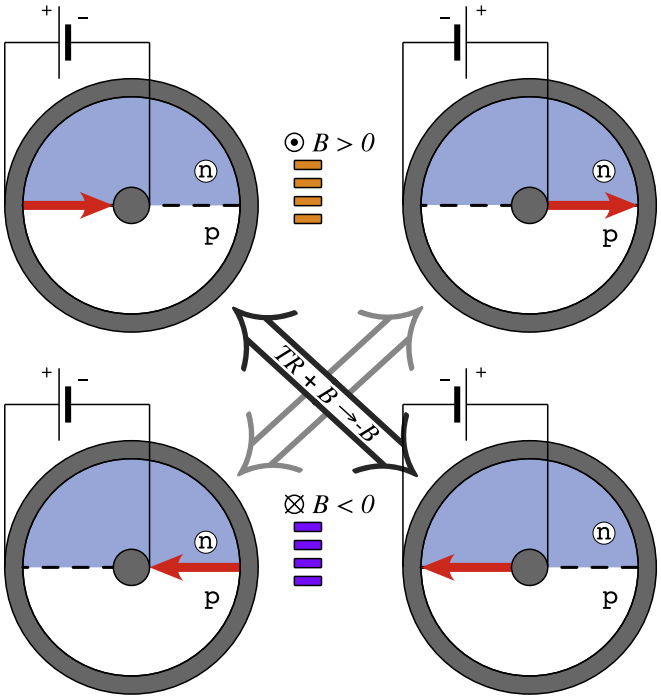

Figure 2. Quantum Hall states propagating along a p–n junction in the strong-field limit, for $B > 0$ (top) and $B < 0$ (bottom). Diagonal double arrows indicate the system symmetry upon a simultaneous time reversal and magnetic field inversion.

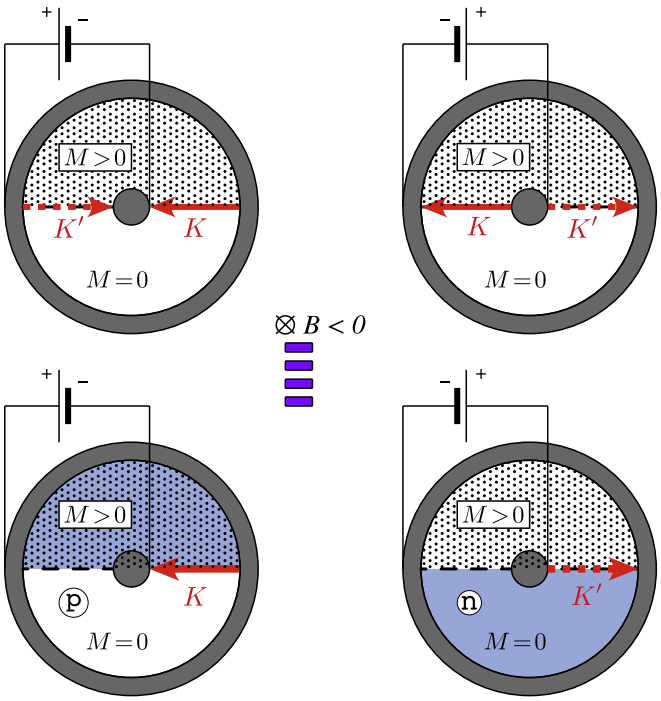

Figure 3. The separation of valley currents (top) and the valley polarization (bottom). A constant staggered potential induces the effective mass $M > 0$ in the upper half of the disk (dotted area). Gate electrodes (not shown) tune the doping in the lower half which is undoped (top), *p*-doped (bottom left), or *n*-doped (bottom right).

time-reversal symmetry in a single valley (*symplectic symmetry*), whereas the magnetic field breaks the *true* time-reversal symmetry (involving the valley exchange). Together, these two symmetry-breaking factors lead to the inequivalence of valleys, providing an opportunity to produce nonequilibrium valley polarization of current.

Referring to the above scenario may also partly explain the valley polarization occurrence in nanobubbles [20, 21], since geometric deformations usually led to a nonzero mass term [44]. However, in such systems,

valley-dependent gauge fields play a dominant role, so an interpretation in terms of basic symmetry breakings is not as clear as in the real magnetic field case considered here.

The paper is organised as follows: in section 2, we briefly present the effective Dirac theory and the transfer matrix approach to the scattering problem in the angular-momentum space (adjusted to the Corbino-disk symmetry). In section 3, we discuss our numerical results concerning the current distribution and valley filtering in the presence of external electromagnetic field and the staggered potential. The conclusions are given in section 4.

2. Model and methods

2.1. The effective Dirac equation

Let us start by considering a ring-shaped sample, characterized by the inner radius R_i and the outer radius R_o, surrounded by metallic contacts modelled by heavily-doped graphene areas (we set $R_o = 4R_i = 200$ nm for all systems considered in the paper). Since we focus on *smooth* (or long-range) disorder, the intervalley scattering can be neglected and one can consider the single-valley Dirac equation

$$(\xi\pi_x\sigma_x + \pi_y\sigma_y)\psi(r,\,\phi) = [E - \mathcal{V}(r,\,\phi) - \mathcal{M}(r,\,\phi)\sigma_z]\psi(r,\,\phi), \tag{1}$$

where $\xi = 1\,(-1)$ is the valley index for K (K') valley, σ_α (with $\alpha = x, y, z$) is the Pauli matrix, $\pi_\alpha/v_F = (-i\hbar\,\partial_\alpha + eA_\alpha)$ is the gauge-invariant momentum operator with $v_F \approx 10^6$ m s^{-1} the Fermi velocity, E denotes the Fermi energy, and $\mathcal{V}(r,\,\phi)$ and $\mathcal{M}(r,\,\phi)$ are position-dependent electrostatic potential energy and mass (respectively) in polar coordinates $(r,\,\phi)$. We choose the symmetric gauge $\boldsymbol{A} = \frac{B}{2}(-y,\,x)$ with a uniform magnetic field B. Furthermore, $B \neq 0$ for the disk area ($R_i < r < R_o$) only; inside the leads ($r < R_i$ or $r > R_o$) we simply set $B = 0$, as the value of B becomes irrelevant in the high-doping limit (see e.g. [34]).

In the case of a system with cylindrical symmetry (namely, $\mathcal{V}$ and $\mathcal{M}$ being ϕ-independent), the Hamiltonian in equation (1) commutes with the angular-momentum operator, $L_z = -i\hbar\,\partial_\phi + \xi\hbar\sigma_z/2$, and the wavefunction can be expressed as a product of radial and angular parts

$$\psi_l(r,\,\phi) = \varphi_l(\phi)\theta_l(r) \equiv e^{i(l-\xi\sigma_z/2)\phi}\begin{bmatrix}\theta_{A,l}(r)\\ \theta_{B,l}(r)\end{bmatrix}, \tag{2}$$

where l is an half-odd integer, and A (B) labels the upper (lower) spinor element.

2.2. Mode-matching in the angular-momentum space

To solve the scattering problem numerically we simplify here, for the case of a monolayer, the method earlier developed for the Corbino disk in bilayer graphene [45].

If $\mathcal{V}$ or $\mathcal{M}$ in equation (1) is ϕ-dependent the cylindrical symmetry is broken, however, one still can employ the angular-momentum eigenfunctions to represent a general solution as a superposition

$$\psi(r,\,\phi) = \sum_k \psi_k(r,\,\phi), \tag{3}$$

with $\psi_k(r,\,\phi)$ given by equation (2) (see also appendix A).

Substituting the above into equation (1) we obtain

$$\sum_k \hbar v_F[\partial_r - f^k(r)]\psi_k(r,\,\phi) = \sum_k \xi\{i\sigma_x[E - \mathcal{V}(r,\,\phi)] - \sigma_y\mathcal{M}(r,\,\phi)\}\psi_k(r,\,\phi), \tag{4}$$

where $f^k(r) = [\xi(k/r + l_B^{-2}r/2)\sigma_z - 1/(2r)\mathbb{I}_{2\times 2}]$, the magnetic length $l_B = \sqrt{\hbar/(eB)}$, and $\mathbb{I}_{n\times n}$ is the $n \times n$ identity matrix. Multiplication over the conjugate angular wavefunction $\varphi_l^*(\phi)$ and subsequent integration over the polar angle ϕ leads to

$$\left[\partial_r - f^l(r) - i\sigma_x\frac{\xi E}{\hbar v_F}\right]\theta_l(r) = \sum_k \xi[-i\sigma_x\mathbb{V}_{lk}(r) - \sigma_y\mathbb{M}_{lk}(r)]\theta_k(r), \tag{5}$$

with

$$\mathbb{V}_{lk}(r) = \frac{1}{2\pi}\int_0^{2\pi} d\phi[\mathcal{V}(r,\,\phi)/(\hbar v_F)]e^{i(k-l)\phi}, \tag{6}$$

and

$$\mathbb{M}_{lk}(r) = \frac{1}{2\pi}\int_0^{2\pi} d\phi[\mathcal{M}(r,\,\phi)/(\hbar v_F)]e^{i(k-l)\phi}. \tag{7}$$

(Notice that the angular dependence of $\mathcal{V}$ or $\mathcal{M}$ introduces the mode-mixing in our scattering problem.)

The general solution of equation (5) can be written as a vector $\boldsymbol{\theta}(r) = [\theta^A_{l_{\min}}(r),\ \ldots,\ \theta^A_{l_{\max}}(r),\ \theta^B_{l_{\min}}(r),\ \ldots,\ \theta^B_{l_{\max}}(r)]^T$, with cutoff angular-momentum quantum numbers

$l_{\min}$ and $l_{\max}$. (Hereinafter, $L = l_{\max} - l_{\min} + 1$ is the total number of transmission modes.) Subsequently, one can write

$$\{[\partial_r + 1/(2r)]\mathbb{I}_{2L\times 2L} - \xi\sigma_z \otimes \mathbb{L}\}\boldsymbol{\theta}(r) = \xi\left[i\frac{E}{\hbar v_F}\sigma_x \otimes \mathbb{I}_{L\times L} - i\sigma_x \otimes \mathbb{V} - \sigma_y \otimes \mathbb{M}\right]\boldsymbol{\theta}(r), \tag{8}$$

where $\mathbb{A} \otimes \mathbb{B}$ is the Kronecker product of matrices $\mathbb{A}$ and $\mathbb{B}$, and the diagonal matrix

$$\mathbb{L} = \mathrm{diag}\left(\frac{l_{\min}}{r} + \frac{r}{2l_B^2}, \frac{l_{\min}+1}{r} + \frac{r}{2l_B^2}, \ \ldots, \ \frac{l_{\max}}{r} + \frac{r}{2l_B^2}\right). \tag{9}$$

Once the scattering matrix is determined (see appendix A for details), transport properties of the system can be calculated within the Landauer–Büttiker formalism in the linear-response regime [46, 47]. In particular, the electrical conductance and valley polarization are given by

$$G = G_0 \sum_{\xi=\pm 1} \mathrm{Tr}\,\mathbf{T}_\xi, \qquad \mathcal{P} = \frac{\mathrm{Tr}\,\mathbf{T}_{\xi=1} - \mathrm{Tr}\,\mathbf{T}_{\xi=-1}}{\mathrm{Tr}\,\mathbf{T}_{\xi=1} + \mathrm{Tr}\,\mathbf{T}_{\xi=-1}}, \tag{10}$$

where $G_0 = 2e^2/h$, the prefactor 2 marks the spin degeneracy (we neglect the Zeeman effect[4]), and $\mathbf{T}_\xi = \mathbf{t}_\xi^\dagger \mathbf{t}_\xi$ with $\mathbf{t}_\xi$ being the transmission matrix for one valley. We further neglect the electron–electron interaction and electron–phonon coupling, which is a common approach to nanosystems in monolayer graphene close to the Dirac point, as the scattering processes associated with these many-body effects are usually slower than the ballistic-transport processes [48, 49].

The matrix $\mathbf{t}$ is also employed when calculating the radial current density, which is given by

$$j_r(r, \phi) = ev_F \sum_l \psi_l^\dagger(r, \phi) J_r(\phi) \psi_l(r, \phi), \tag{11}$$

with the radial current density operator

$$J_r(\phi) = \xi\sigma_x \cos\phi + \sigma_y \sin\phi, \tag{12}$$

and $\psi_l(r, \phi) = \sum_k (\mathbf{t}_\xi)_{l,k}\, e^{i(k-\xi\sigma_z/2)\phi}(1, \xi)^T/\sqrt{r}$ being the transmitted wavefunction in the outer contact ($r > R_o$). The matrix element $(\mathbf{t}_\xi)_{l,k}$ denotes the transmission probability amplitude from channel k to l. Similarly, the Cartesian components of the current density $\boldsymbol{j}(r, \phi) = (j_x, j_y)$ are calculated by replacing the operator J_r in equation (11) by

$$J_x = \xi\sigma_x \quad \text{or} \quad J_y = \sigma_y \quad \text{(respectively)}. \tag{13}$$

3. Quantum transport in crossed electric and magnetic fields

3.1. Definitions

In order to study a role of the p–n junction in quantum transport through graphene-based Corbino disk, we choose the electrostatic potential energy as follows

$$\mathcal{V}(r, \phi) = -e\mathcal{E}r \sin(\phi - \phi_V), \tag{14}$$

where $\mathcal{E}$ is the electric field (we further define $V \equiv e\mathcal{E}R_o$) and the angle ϕ_V defines the crystallographic orientation of the p–n interface [50, 51]. Furthermore, we investigate how the transport is affected by the mass term

$$\mathcal{M}(r, \phi) = M\Theta(\phi - \phi_M)\Theta(\pi + \phi_M - \phi), \tag{15}$$

with the angle ϕ_M specifying the mass arrangement, and $\Theta(x)$ being the Heaviside step function. The mass term given by equation (15) is restricted to a half of the disk, $\phi \in [\phi_M, \pi + \phi_M]$, see figure 4. In the heavily-doped contact regions, $\mathcal{V}(r, \phi) = \mathcal{M}(r, \phi) = 0$.

It is worth to mention that we have also considered other functional forms of the mass term, including $\mathcal{M}(r, \phi)$ smoothly varying with the distance from a p–n junction, always finding a parameter range in which the valley-filtering mechanism that we describe was highly efficient. Even for a simple model given by equation (15), changing the Fermi energy (E) allows one to shift a p–n interface ($E - \mathcal{V}(r, \phi) = 0$) with respect to the mass boundary, leading to a rich phase diagram discussed later in this section.

The specific forms of the potential energy $\mathcal{V}(r, \phi)$ and the mass term $\mathcal{M}(r, \phi)$, given by equations (14) and (15), lead to the matrix elements

[4] For $B = 1$ T the Zeeman splitting is $\Delta E_Z = g\mu_B B \approx 0.1$ meV [with $g \approx 2$ and $\mu_B = e\hbar/(2m_e)$ the Bohr magneton] and cannot affect the filter operation appearing at the potential and mass-term amplitudes of $V \sim M \gtrsim 10$ meV.

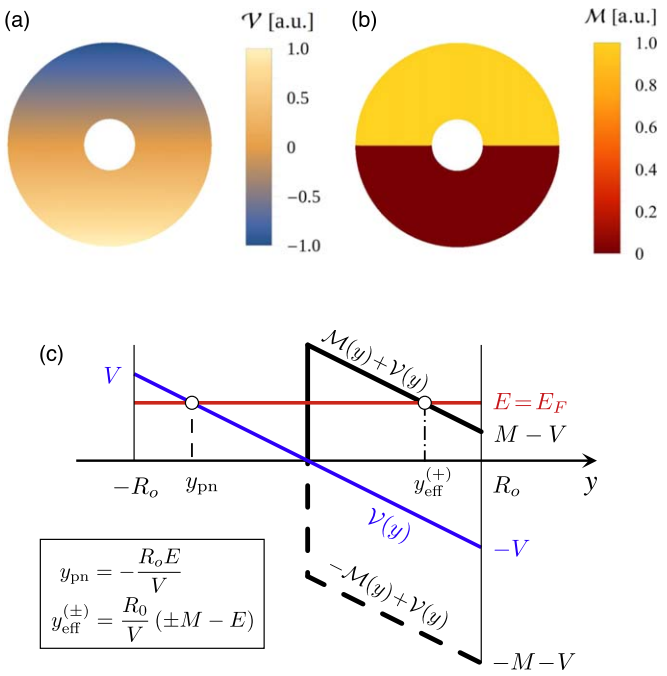

Figure 4. (a) Electrostatic potential energy $\mathcal{V}(r,\,\phi)$ given by equation (14) with $\phi_V = 0$, corresponding to a homogeneous electric field $\mathbf{E} = (0,\,\mathcal{E})$. (b) The mass term $\mathcal{M}(r,\,\phi)$ given by equation (15) with $\phi_M = 0$ (i.e. $\mathcal{M} = M \neq 0$ in the upper half of the disk only). (c) Cross sections of the electrostatic potential energy $\mathcal{V}(y)$ (blue line) and the effective potentials $\mathcal{V}(y) \pm \mathcal{M}(y)$ (black solid or dashed line) along the disk diameter: $x = 0$, $-R_o \leqslant y \leqslant R_o$, for some $V, M > 0$. Red line marks the Fermi energy E. The expressions for $y_{\rm pn}$ (the position of a p–n interface), following from $\mathcal{V}(y_{\rm pn}) = E$, and $y_{\rm eff}^{(\pm)}$ (for which $\mathcal{V} \pm \mathcal{M} = E$) are also given. (The inner-lead edges, $y = \pm R_i$, are omitted for clarity.)

$$\mathbb{V}_{lk} = -\delta_{|l-k|,1}\frac{Vr\pi}{hv_F R_o}\, i^{k-l} \exp\left[i(k-l)\phi_V\right], \tag{16}$$

and

$$\mathbb{M}_{lk} = \frac{Mr}{hv_F R_o}\begin{cases}\pi & \text{if } |l-k| = 1,\\ i\frac{1-(-1)^{k-l}}{k-l}\mathrm{e}^{i(k-l)\phi_M} & \text{if } |l-k| \neq 1.\end{cases} \tag{17}$$

3.2. Quantum Hall regime in the massless case

We consider now the case of $M = 0$ in equation (15). The Fermi energy is set as $E = 0$ and thus the p–n interface overlaps with the disk diameter ($y_{\rm pn} = 0$) for any $V \neq 0$.

For moderate values of the electric field ($|V| < 10$ meV) and weak magnetic fields the magnetoconductance behavior is the same as in a case without the p–n junction [34], see figure 5. The increase of G at weak magnetic fields, visible for $|V| = 10$ meV, indicates the system is close to the ballistic transport regime. This occurs when the (position-dependent) cyclotron diameter $2r_c(0,\,y) \gtrsim R_o - R_i$, enhancing vertical currents along the classical trajectories (see the top panel in figure 1). For our choice of the parameters, the cyclotron radius,

$$r_c(x,\,y) = \frac{|E - \mathcal{V}(x,\,y)|}{eBv_F}, \tag{18}$$

is bounded by $r_c(0,\,y) \geqslant (R_i/R_o)|V|/(eBv_F)$ along the vertical diameter ($x = 0$) and for $R_i \leqslant |y| \leqslant R_o$.

Another apparent feature of the data presented in figure 5 is a rapid conductance drop, occurring for any $V \neq 0$ at sufficiently high field. Unlike in a uniformly-doped disk out of the charge-neutrality point, where G vanishes in the high-field limit [34], here G approaches the value of $4e^2/h$ (i.e. the *conductance quantum* with spin and valley degeneracies) signalling the crossover from pseudodiffusive to quantum-hall transport regime. The limiting value of G reproduces the experimental result of [36], and can be easily explained by analysing symmetries of the Dirac theory [52].

A bit more detailed view of the effect is provided with the evolution of angle-dependent current density at the outer disk edge ($r = R_o$) with increasing field, presented in figure 6(a). We choose a high electric field ($V = 50$ meV) to ensure the system undergoes a crossover directly from ballistic to quantum-Hall transport regime, as the contribution from evanescent waves is negligible. For $B = 0$ (red line) the current flows in directions along which the doping is extremal, namely, $\phi = \pm\pi/2$. For higher fields the transport is dominated

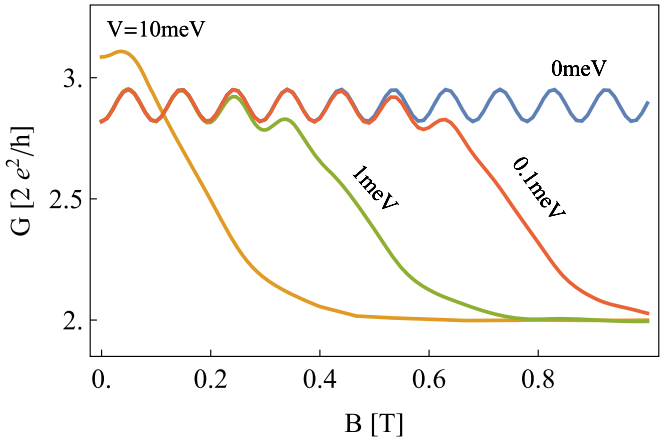

Figure 5. Magnetoconductance of the Corbino disk with $R_o = 4R_i = 200$ nm, $E = M = 0$, and different values of the in-plane electric field $\mathcal{E}$ (quantified by $V \equiv e\mathcal{E}R_o$). Notice that the conductance (G) approaches the one quantum value ($4e^2/h$) for any $V \neq 0$ at sufficiently high magnetic field (B).

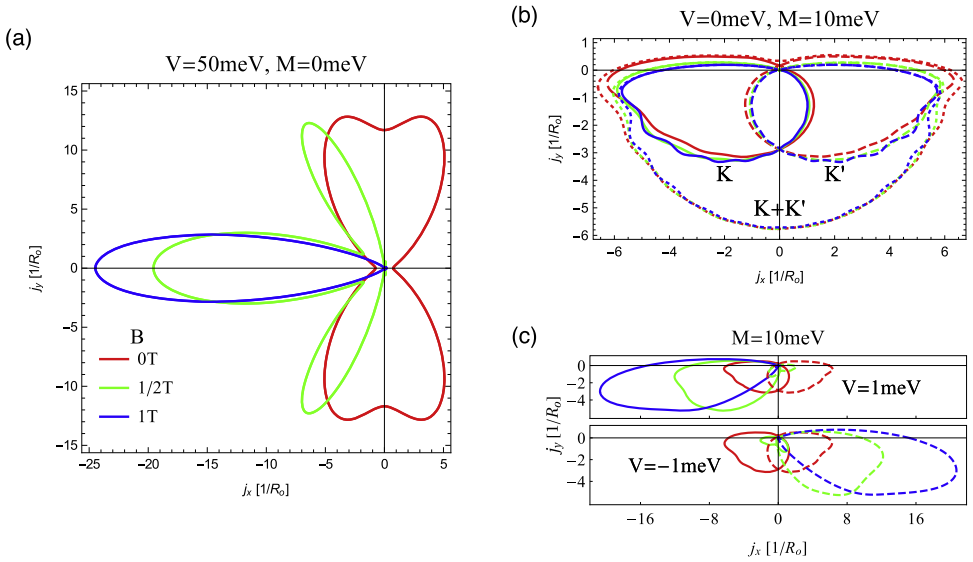

Figure 6. Parametric plots of the current density $\boldsymbol{j}(r, \phi)|_{r=R_o} \equiv (j_x, j_y)$ [see equation (13)], where $0 \leqslant \phi < 2\pi$, for the same setup as in figure 5 with the electrostatic potential and mass magnitudes (V and M) varied between the subplots. Line colours (same for each subplot) mark different magnetic fields: $B = 0$ (red), $B = 1/2$ T (green), and $B = 1$ T (blue). (a) For $M = 0$, the results are identical for both valleys. A relatively large value of $V = 50$ meV eliminates the pseudodiffusive charge-transport regime. At 1 T field, the distribution resembles the analytical result for an infinite plane with the p–n junction, see figure B2 in appendix B. (b) For $V = 0$ and $M = 10$ meV, the separation of valley currents appears. Solid and dashed lines correspond to distinct contributions from the two valleys (K, K'); dotted lines depict the current density summarized over the valleys ($K + K'$). (c) For $M = 10$ meV and $V = \pm 1$ meV (top/bottom panel), polarity of the p–n junction allows one to select one of the valley currents and suppress the other. (The summarized current density is omitted for clarity.)

by a single direction, for which $\mathcal{V}(r, \phi) = 0$ (i.e. $\phi = \pi$), with some secondary currents at $|\phi| \lesssim \pi/2$ visible for $B = 1/2$ T (green line), and vanishing for $B = 1$ T (blue line). This picture is in agreement with the results of previous theoretical studies (see [52] and appendix B for details).

As the magnetic length at 1 Tesla field $l_B(B = 1\ \mathrm{T}) \approx 26$ nm is still comparable with the system size (in particular, the inner radii $R_i = 50$ nm), the transport cannot be understood classically or quasiclassically. Therefore, several features depicted schematically in figure 1 (such as the orbits in the middle panel) have no correspondants in numerical results presented in figure 6(a). However, an apparent asymmetry of the current distribution for $B \neq 0$ is directly linked to the left-right mirror symmetry breaking, also present in the classical level: both the trajectories and quantum-hall edge states are symmetric upon a simultaneous left-right reflection and the field inversion (see figure 2); the same applies to the voltage-source polarity (or time) reversal combined with the magnetic field inversion.

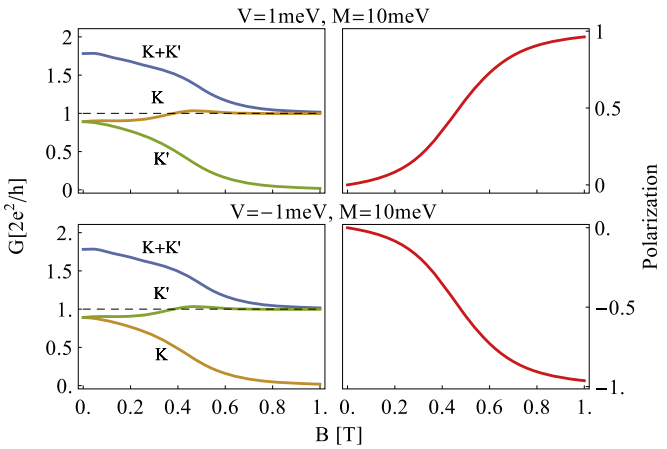

Figure 7. Conductance (left) and valley polarization (right) defined by equation (10) for the Corbino disk with both the mass term and the p–n interface displayed as functions of the magnetic field. Remaining system parameters are same as in figure 6(c).

3.3. Mass term and the valley filter operation

So far, we have put $M = 0$ in equation (15) and the transport characteristics were identical for both valleys (K and K'). A different picture emerges in the system with nonzero and spatially-varying mass term (the $M \neq 0$ case). Our simplified model, in which the mass is present only in the upper half of the system (see figure 4), already allows to demonstrate the mesoscopic valley-filtering mechanism. In this subsection, we present the central results of the paper, providing a quantitative description of the effects depicted schematically in figure 3.

Quite surprisingly, even at zero electric and magnetic fields the currents corresponding to different valleys are well separated (see figure 6(b)). This can be interpreted as a zero-doping version the edge-state formation (the Fermi energy is fixed at $E = 0$). As the mass opens a band gap in the upper half of the disk ($0 < \phi < \pi$), there are no extended states available, and the current is pushed away towards the lower half ($-\pi < \phi < 0$). In turn, the border between areas with $\mathcal{M} = 0$ and $\mathcal{M} \neq 0$ plays a role of an artificial edge of the system (notice that the p–n junction is absent for $V = 0$). The *total* current distribution (dotted lines in figure 6(b)) is approximately uniform in the lower half of the disk (as this part is in the pseudodiffusive charge-transport regime), with some local maxima for $\phi \approx 0$ and $\phi \approx -\pi$, signaling contributions from the zero-energy edge states. The emergence of such states is well-described in graphene literature, see e.g. [53]; their analogs in bilayer graphene in a position-dependent perpendicular electric field were also discussed [25]. A basic reasoning why electrons in different valleys prefer opposite directions of propagation is given in appendix C.

A direct link between the valley polarization of current and the direction of propagation for zero-energy edge states leads to the spatial separation of valley currents, which is apparent even in our relatively small system, for which the role of evanescent waves is still significant (and manifests itself by a nonzero current density for any $-\pi < \phi < 0$).

Next, the valley-filtering mechanism is demonstrated by creating the p–n interface in a presence of the mass term ($V \neq 0$, $M \neq 0$). Figure 6(c) shows a strong suppression of one of the valley currents in relatively weak electric and magnetic fields (and the valley is selected by a *sign* of V), provided that the mass term is sufficiently strong. The valley polarization $\mathcal{P}$ gradually increases with the magnetic field, becoming almost perfect for $B = 1$ T (see figure 7).

The operation of our valley filter is characterized in details by the numerical results presented in figure 8, where we have fixed $V = 1$ meV, and visualized the transport characteristics in the Fermi energy-mass (E–M) parameter plane, for three selected values of the magnetic field ($B = 0$, 1/2, and 1 T). Notice that varying E corresponds to a vertical shift of the p–n interface; in particular, for $E = VR_i/R_o = 0.25$ meV we have $y_{\mathrm{pn}} = -R_i$ (see figure 4) and the p–n interface is a tangent line to the inner disk edge at the lower (i.e. mass-free) half. At zero magnetic field, the density maps shown in bottom panels are perfectly uniform, and no valley polarization is visible. For higher fields, distinct regions of the 'phase diagram' are formed, including the unpolarized highly-conducting region ($G \approx 2G_0$, $\mathcal{P} \approx 0$) at the central-bottom part of each subplot, the two polarized highly-conducting regions ($G \approx G_0$, $\mathcal{P} \approx \pm 1$) near the upper corners, and the two tunneling regions ($G \approx 0$, $\mathcal{P} \approx 0$) near the lower corners. At 1 T field (top panels), the boundaries between above-mentioned regions are already well-developed.

Some further insights into relations connecting the diagram structure and characteristic features of the effective potential profile, $\mathcal{V}(r, \phi) \pm \mathcal{M}(r, \phi) \equiv \mathcal{V}(y) \pm \mathcal{M}(y)$ in equation (1), are given in figure 9. In brief, the boundaries between regions on the E–M diagram can be attributed to the situations when the p–n line is

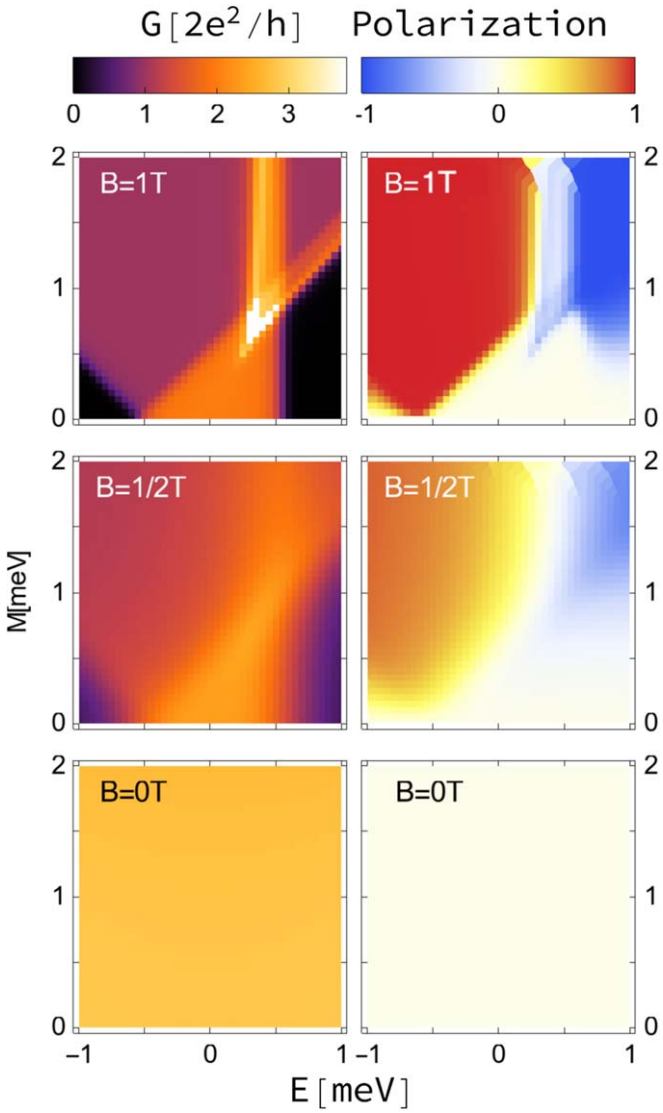

Figure 8. Conductance (left) and valley polarization (right) for $V = 1$ meV as functions of the Fermi energy (E) and the mass term (M). The value of magnetic field (B) is varied between the panels. Remaining system parameters are same as in figure 5.

a tangent to the inner disk edge at the mass-free part, $y_{\mathrm{pn}} = -R_i$ (vertical dashed line), or when the Fermi energy is equal to the effective potential along a tangent line to the inner disk edge at the nonzero mass part, $y_{\mathrm{eff}}^{(\pm)} = R_i$ (diagonal solid lines). The sketch of figure 9 corresponds to the high-field limit, in which $l_B \ll R_i$ and varying E may lead to an abrupt switching between the regions. In a finite-field situation (see figure 8), finite widths of quantum Hall states result in blurs (and shifts) of the boundaries, with a general trend to expand the unpolarized highly-conducting region with decreasing B.

Numerous experimental realizations of a non-uniform mass in monolayer graphene [39–43] suggest to focus on a constant and relatively large $M \gg 1$ meV. In such a case, the magnetic field of $B = 1$ T allows one to control the valley polarization of current independently by tuning the Fermi energy (E) or by reversing the p–n junction polarity ($V \to -V$).

It is also worth stressing, that high valley polarization remains unaffected when the p–n interface is moved by a distance of $\Delta y \approx R_i = 50$ nm away from the mass boundary, allowing us to coin the term of mesoscopic valley filter.

4. Conclusions

We have demonstrated, as a proof of principle, that the Corbino disk in monolayer graphene modified such that the mass term in effective Dirac equation is present in a half of the disk (leading to the energy gap of $\gtrsim 1$ meV) may act as a highly efficient valley filter, when placed in crossed electric and magnetic fields inducing a p–n interface close to the mass-region boundary. Although introducing the mass term involves a microscopic

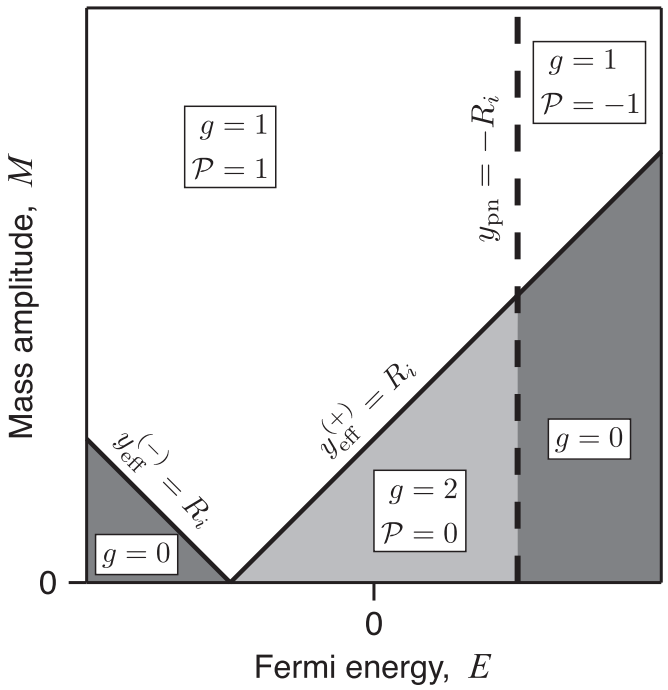

Figure 9. Sketch of the high-field 'phase diagram' for some $V > 0$ (see top panel in figure 8) with distinct regions characterized by dimensionless conductance $g = G/G_0$ and the polarization $\mathcal{P}$, with the boundaries given by mutual relation between the Fermi energy and the potentials ($\mathcal{V} \pm \mathcal{M}$ and $\mathcal{V}$) at the inner disk edge: $y_{\rm eff}^{(\pm)} = R_i$ (solid lines) and $y_{\rm pn} = -R_i$ (dashed line). (See also figure 4(c)).

modification of a sample, the output (valley) polarization of current may be controlled electrostatically in constant magnetic field, alternatively by: (i) inverting the p–n junction polarity, or (ii) shifting the p–n line with respect to the mass boundary by tuning a global doping of a sample. The magnetic field of 1 T is sufficient to obtain the polarization better than 99% for the device size (namely: the outer disk diameter) of 400 nm.

An additional interesting feature of the system is that the currents belonging to different valleys are spatially separated, flowing in opposite directions along the p–n interface. In the absence of a p–n interface, there are two equal currents propagating along the mass boundary; in-plane electric field amplifies one of these currents and suppresses the other. The filtering mechanism is directly linked to global symmetry breakings of the Dirac Hamiltonian, and therefore we expect it to be robust against typical perturbations in real experiments.

For instance, the operation of mesoscopic valley filter which we have described should not be noticeably affected by the long-range (or smooth) impurities, as they generally do not introduce the intervalley scattering [54, 55]. (In contrast, short-range impurities mix the valleys and may restore the equilibrium valley occupation.) Recent experimental works on ultraclean graphene p–n junctions [31, 32] allow us to believe that such systems, accordingly modified to induce a position-dependent quasiparticle mass, may also act as highly-efficient mesoscopic valley filters. Since the valley filtering takes place in a proximity of the p–n interface, which can be shifted (or bent) during an experiment by using external gates, we anticipate that more complex multiterminal geometry will make it possible to setup a few filters in series in order to independently produce and detect valley-pseudospin polarization by means of nonlocal measurements. Numerical simulations for the multiterminal geometry are, however, beyond the scope of this paper.

Acknowledgments

Discussions with Piotr Witkowski are appreciated. The work was supported by the National Science Centre of Poland (NCN) via Grant No. 2014/14/E/ST3/00256. Computations were partly performed using the PL-Grid infrastructure.

Appendix A. Transfer matrix approach

A general wavefunction corresponding to the lth transmission channel is given by a linear combination of two linearly-independent spinor functions

$$\theta^l(r) = a_1^l\theta_1^l(r) + a_2^l\theta_2^l(r), \tag{A1}$$

where a_α^l ($\alpha = 1, 2$) are arbitrary complex amplitudes and $\theta_\alpha^l(r) = [\theta_{\alpha,A}^l, \theta_{\alpha,B}^l]^T(r)$ is a normalized spinor function with A and B being the sublattice indices. The normalization has to be carried out in such a way that the total current remains constant (i.e. l, α–independent). To satisfy this condition, we write down the current density for the lth transmission channel

$$\vec{j_l} = ev_F[\theta^l(r)]^\dagger \cdot [\xi\sigma_x\cos(\varphi) + \sigma_y\sin(\varphi)] \cdot \theta^l(r). \tag{A2}$$

In principle, it is sufficient to normalize only the wavefunctions in the leads since the relation between them (namely: between the incoming, the transmitted, and the reflected wavefunction) ultimately defines matrices $\mathbf{r}$ and $\mathbf{t}$. Current conservation guarantees that amplitudes r_{mn} and t_{mn} preserve the probabilistic interpretation. Therefore, a direct normalization for the wavefunctions in the sample area is not essential for the successful mode matching.

Next, it is convenient to present a complete set of wavefunctions as a vector with each element corresponding to a different transmission channel. Since only a limited number of channels contributes significantly to the quantum transport, one can look for a truncated solution by introducing the cutoff-transmission channels $l_{\min}$ and $l_{\max}$ such that $l \in [l_{\min}, l_{\max}]$. The total number of transmission channels, $M = (l_{\max} - l_{\min} + 1)$, is chosen to be large enough to reach the convergence. In such a notation, we can write

$$\boldsymbol{\theta}(r) = \mathbb{M}(r)\begin{pmatrix}\boldsymbol{a}_1\\ \boldsymbol{a}_2\end{pmatrix}, \tag{A3}$$

where $\mathbb{M}(r)$ is a $2M \times 2M$ matrix, $\boldsymbol{a}_\alpha = [a_\alpha^{l_{\min}}, \ldots, a_\alpha^{l_{\max}}]^T$. The explicit form of matrix $\mathbb{M}(r)$ will be presented later. The notation of equation (A3) is convenient when dealing with a system with mode mixing introduced by a position-dependent potential.

We are primarily interested in a relation between the two sets of amplitudes defining wavefunctions at different radii, say: r and R_i. Such a relation can be written introducing a propagator $\mathbb{U}(r, R_i)$,

$$\boldsymbol{\theta}(r) = \mathbb{U}(r, R_i)\boldsymbol{\theta}(R_i). \tag{A4}$$

The propagator $\mathbb{U}(r, R_i)$ can be found by substituting equations (A4) into (8) from the main text (the Dirac equation). The resulting equation takes the following form

$$\partial_r\mathbb{U}(r, R_i) = \mathbb{A}(r)\mathbb{U}(r, R_i), \tag{A5}$$

with an initial condition $\mathbb{U}(R_i, R_i) = \mathbb{I}_{2M\times 2M}$. The matrix $\mathbb{A}(r)$ in equation (A5) carries the complete information about the potential and the mass term in the system.

Formally, equation (A5) defines $2M$ independent systems of $2M$ ordinary differential equations, each of which describing a column in the matrix $\mathbb{U}(r, R_i)$. We have employed a fixed-step explicit Runge Kutta method of the 4th order [56]. Both the step-size as well as the number of transmission channels M are adjusted to reach the numerical convergence; in practice, these parameters depend on the system size, as well as on the magnetic field, in an approximately linear manner similarly as in the case of bilayer graphene (see [45]).

Once the propagator for the sample area $\mathbb{U}(R_o, R_i)$ is determined, we can translate it onto a transfer matrix, connecting the wavefunctions in the leads with wavefunctions in the sample area, via the mode-matching

$$\begin{aligned}\boldsymbol{\phi}^L(R_o) &= \boldsymbol{\phi}^S(R_o)\\ &= \mathbb{U}(R_o, R_i)\boldsymbol{\phi}^S(R_i)\\ &= \mathbb{U}(R_o, R_i)\boldsymbol{\phi}^L(R_i),\end{aligned} \tag{A6}$$

where $\boldsymbol{\phi}^L(R_o) = \mathbb{M}_L(r)\boldsymbol{a}$. As the doping in the leads is set to infinity, the matrix $\mathbb{M}_L(r)$ can be presented as a Kronecker product $\mathbb{M}_L(r) = \mathbb{B}(r) \otimes \mathbb{I}_{M\times M}$ (we have omitted the phase constants as they are insignificant when calculating the transport properties), where

$$\mathbb{B}(r) = \frac{1}{\sqrt{r}}\begin{bmatrix}1 & 1\\ \xi & -\xi\end{bmatrix}. \tag{A7}$$

Columns in the matrix $\mathbb{B}(r)$ represents independent wavefunctions, corresponding to different directions of propagation (incoming and outgoing waves). The transfer matrix is thus given by

$$\mathbb{T} = \mathbb{M}_L^{-1}(R_o)\mathbb{U}(R_o, R_i)\mathbb{M}_L(R_i). \tag{A8}$$

Finally, the transmission properties of the system can be obtained by retrieving the scattering-matrix elements from $\mathbb{T}$. The transfer matrix can be expressed by blocks of the scattering matrix as follows

$$\mathbb{T} = \begin{bmatrix}(\mathbf{t}^\dagger)^{-1} & \mathbf{r}'\cdot(\mathbf{t}')^{-1}\\ -(\mathbf{t}')^{-1}\cdot\mathbf{r}' & (\mathbf{t}')^{-1}\end{bmatrix}, \tag{A9}$$

where **t** and **r** are the transmission and reflection matrix (respectively) for a wavefunction incoming from the inner lead; similarly, **t′** and **r′** are the transmission and reflection matrix for a wavefunction incoming from the outer lead.

Appendix B. Solutions for an infinite graphene plane

The clear asymmetry of a current propagating along the p–n junction in the quantum Hall regime (see figure 6(a) in the main text) illustrate an intrinsic feature that is not related to the Corbino geometry. In this appendix we derive analytically the eigenfunctions for the low-energy Hamiltonian of graphene in crossed electric and magnetic fields

$$H = \begin{pmatrix} -e\mathcal{E}x & \xi\pi_x - i\pi_y \\ \xi\pi_x + i\pi_y & -e\mathcal{E}x \end{pmatrix}, \tag{B1}$$

where $\pi_\alpha = -i\hbar\partial_\alpha + eA_\alpha$ with the Landau gauge $\mathbf{A} = (0,\ Bx)$, and the mass term is neglected for simplicity. (Notice that the electrostatic potential energy term in equation (B1) corresponds to $\phi_V = \pi/2$ in equation (14)). It is clear now that the Hamiltonian (B1) is invariant under the time reversal combined with the magnetic field inversion, namely

$$H(-\xi,\ -B) = \mathcal{T}_\xi H(\xi,\ B)\mathcal{T}_\xi^{-1}, \tag{B2}$$

where $\mathcal{T}_\xi = \sigma_0\mathcal{C}$ is a single-valley time reversal operator with $\mathcal{C}$ denoting complex conjugation. (In the four-component notation, the full time reversal is $\mathcal{T} = \tau_x \otimes \mathcal{T}_\xi$, where τ_x is the Pauli matrix acting on valley degrees of freedom.)

Due to the translation symmetry in the y-direction, H (B1) also commutes with $-i\hbar\partial_y$ and thus we can choose the wavefunction as $\Psi(x,\ y) = \Phi(x)\exp(ik_y y)$, with the wavenumber k_y, reducing the scattering problem to a single-dimensional one. The corresponding Dirac equation reads

$$\begin{bmatrix} \frac{e\mathcal{E}}{i\hbar v_F}x & \xi\partial_x + k_y + \frac{eB}{\hbar}x \\ \xi\partial_x - k_y + \frac{eB}{\hbar}x & \frac{e\mathcal{E}}{i\hbar v_F}x \end{bmatrix}\Phi(x) = \frac{iE}{\hbar v_F}\Phi(x). \tag{B3}$$

One can further simplify the above equation introducing the dimensionless variable $\chi = l_B^{-1}x + l_B k_y$, where $l_B = \sqrt{\hbar/e|B|}$ is the magnetic length. Without loss of generality, we can suppose that $B > 0$. Equation (B3) can now be written as

$$\begin{bmatrix} -\gamma\chi & -i(\xi\partial_\chi + \chi) \\ -i(\xi\partial_\chi - \chi) & -\gamma\chi \end{bmatrix}\Phi(x) = \varepsilon\Phi(x), \tag{B4}$$

where we have defined $\gamma = el_B^2\mathcal{E}/(\hbar v_F)$ and $\varepsilon = l_B[E/(\hbar v_F) - \gamma k_y]$. When considering an infinite graphene plane we can choose (without loosing the generality) the zero Fermi energy ($E_F = 0$), what leads to

$$\varepsilon = -l_B\gamma k_y. \tag{B5}$$

Following [57, 58], we find the solutions of equation (B4) by solving an auxiliary eigensystem

$$\mathcal{H}\varphi(x) = \varepsilon^2\varphi(x) \tag{B6}$$

for the operator

$$\mathcal{H} = \varepsilon(H + \tilde{H}) - H\tilde{H}, \tag{B7}$$

where $\tilde{H} = \sigma_z H\sigma_z$, which is chosen such that each eigenfunction of $\mathcal{H}$ satisfies equation (B4) as well. Equation (B6) can rewritten as follows

$$\begin{pmatrix} -O_- & i\xi\gamma \\ i\xi\gamma & -O_+ \end{pmatrix}\begin{pmatrix} u \\ v \end{pmatrix} = \varepsilon^2\begin{pmatrix} u \\ v \end{pmatrix}, \tag{B8}$$

where $O = 2\varepsilon\gamma\chi + \varepsilon^2 - (1-\gamma^2)\chi^2 + \partial_\chi^2 \pm \xi$, and u, v are spinor elements of the wavefunction $\varphi(x)$.

We can now write down the fourth-order differential equation for u, namely

$$\gamma^2 u + O_+O_-u = 0, \tag{B9}$$

being equivalent to the set of two second-order equations

$$\sqrt{1-\gamma^2}\ u_\pm = \pm[2\gamma\varepsilon\chi + \varepsilon^2 - (1-\gamma^2)\chi^2 + \partial_\chi^2]u_\pm. \tag{B10}$$

The solutions are

$$u_{\pm} = a^{\pm} \mathrm{D}_{-(1\pm1)/2+w}(\rho) + b^{\pm} \mathrm{D}_{-(1\mp1)/2-w}(i\rho), \tag{B11}$$

where $\mathrm{D}_{\nu}(x)$ is the parabolic cylinder function [59], $\rho = \sqrt{2}\,(\chi - \gamma^2\chi - \gamma\varepsilon)(1-\gamma^2)^{-3/4}$, $w = \varepsilon^2(1-\gamma^2)^{-3/2}/2$, and $a^{\pm}$, $b^{\pm}$ are arbitrary constants. Since we are interested in square-integrable wavefunctions, we set $b^{\pm} = 0$. Using equation (B8), we obtain the full form of the spinor function

$$\begin{pmatrix} u_{\pm} \\ v_{\pm} \end{pmatrix} = a^{\pm} \mathrm{D}_{-(1\pm1)/2+w}(\rho) \times \begin{bmatrix} 1 \\ i(1 \pm \xi\sqrt{1-\gamma^2})/\gamma \end{bmatrix}. \tag{B12}$$

Both the solutions $(u_+,\, v_+)^T$ and $(u_-,\, v_-)^T$, as well as their arbitrary linear combination, satisfy equation (B8). Therefore, we construct an eigenfunction of equation (B6), corresponding to an eigenvalue $\varepsilon^2 > 0$, by taking [60]

$$\varphi_{\varepsilon^2>0}(x) \equiv \begin{pmatrix} u \\ v \end{pmatrix} = A\left[c \begin{pmatrix} u_+ \\ v_+ \end{pmatrix} + \begin{pmatrix} u_- \\ v_- \end{pmatrix} \right], \tag{B13}$$

where $c = \varepsilon[1 + \xi\sqrt{1-\gamma^2}]/[\sqrt{2}\gamma(1-\gamma^2)^{3/4}]$, and A is the normalization constant

$$A = \sqrt{\frac{(1-\gamma^2)^{1/4}\gamma^2(4\sqrt{\pi}\,l_B)^{-1}}{\Gamma[1+w](1+\xi\sqrt{1-\gamma^2})}}. \tag{B14}$$

The case of $\varepsilon^2 = 0$ (the *zero mode*) is slightly different, and it is instructive to consider it separately. The corresponding solution of equation (B6) reads

$$\varphi_{\varepsilon^2=0}(x) = C e^{-\sqrt{1-\gamma^2}\chi^2/2} \begin{pmatrix} i\frac{\xi\sqrt{1-\gamma^2}-1}{\gamma} \\ 1 \end{pmatrix}, \tag{B15}$$

with

$$C = \sqrt{\frac{\gamma^2(1-\gamma^2)^{1/4}}{2\sqrt{\pi}(1+\xi\sqrt{1-\gamma^2})\,l_B}}. \tag{B16}$$

In a general case, the normalization of $\varphi(x)$ leads also to a discrete spectrum of eigenvalues

$$\varepsilon_n^2 = 2(1-\gamma^2)^{3/2}\, n, \tag{B17}$$

with $n = 0, 1, 2, \ldots$; see [50, 57, 58]. The above, together with equation (B5), implies the wavenumber quantization

$$k_y^{(n)} = \pm\frac{\sqrt{2(1-\gamma^2)^{3/2}n}}{\gamma\, l_B}. \tag{B18}$$

We further notice that the zero mode ($n = 0$) lacks the additional twofold degeneracy of higher modes ($n > 0$).

Explicit forms of wavefunctions, given above by equations (B13) and (B15), allows one to calculate the probability density $|\varphi(x)|^2$ (see figure B1) as well as the local current density $j_y = \varphi^{\dagger}(x) \cdot \sigma_y \cdot \varphi(x)$ (see figure B2).

As we have neglected the mass term throughout this Appendix, the physical quantities displayed in figures B1 and B2 are same for both valleys, K and K', indicated by $\xi = 1$ or $\xi = -1$ (respectively) in equation (B1). Also, the probability density $|\varphi(x)|^2$ is affected by the direction of electric field, indicated by $\mathrm{sgn}\,\mathcal{E} \equiv \mathrm{sgn}\,\gamma$, only in a way that the two solutions for $n > 0$, characterized by opposite wavenumbers (k_y and $-k_y$) are exchanged upon $\gamma \to -\gamma$, see figure B1. In contrast, the current density $j_y(x)$ also changes sign upon $\gamma \to -\gamma$, see figure B2. Revisiting the derivation for $B < 0$, one quickly can find that $|\varphi(x)|^2$ and $j_y(x)$ are affected by the magnetic field inversion ($B \to -B$) at fixed γ in the same way as by the electric field inversion ($\gamma \to -\gamma$) at fixed B.

Another striking feature of the results presented in figure B2 is that for either the $n = 0$ or $n > 0$ modes, the total current (integrated over x) flows in one direction only, determined by the signs of $\mathcal{E}$ and B. For $n > 0$, this can be attributed to the fact that solutions with $k_y > 0$ and $k_y < 0$ are localized at the opposite sides of a p–n interface, resulting in the *same* sign of the group velocity. For $n = 0$, the solution given by equation (B15) can be regarded as a linear combination of edge states from both sides of the interface, for which the current density is centered precisely at the interface line (as depicted schematically in figure 2 in the main text).

We now comment on the relation between solutions for an infinite plane with trajectories depicted in figure 1.

The snake states (bottom panel in figure 1) can be represent as linear combinations of the solutions with $n = 0$ and $n > 0$, having a property that the full combination propagates in the same direction as each of its components. On the other hand, classical trajectories propagating in the direction (approximately)

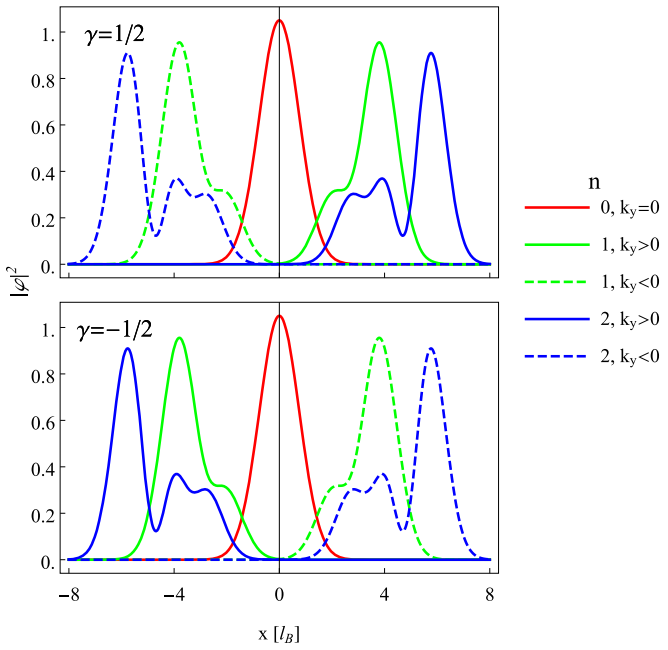

Figure B1. Probability density $|\varphi(x)|^2$ for $\xi = 1$ (the K valley), $B = 1$ T, and $\gamma = 1/2$ (top) or $\gamma = -1/2$ (bottom).

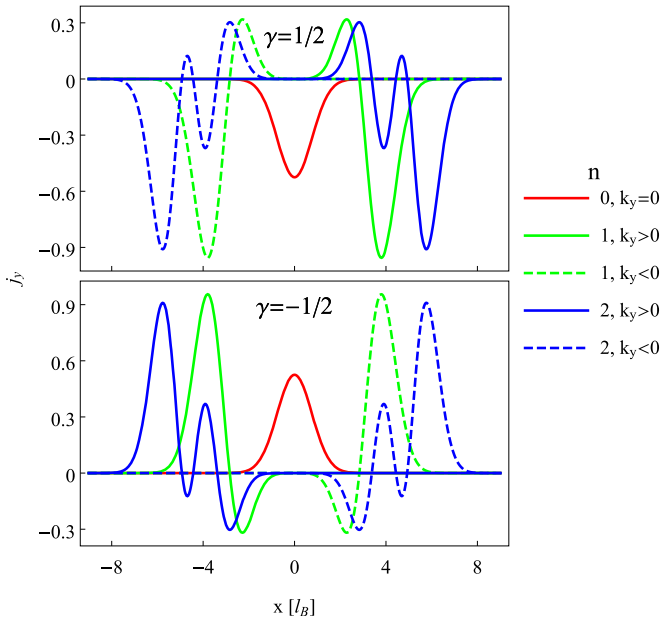

Figure B2. Current density $j_y(x)$ for $\xi = 1$ (the K valley), $B = 1$ T, and $\gamma = 1/2$ (top) or $\gamma = -1/2$ (bottom).

perpendicular to the interface (top panel in figure 1) represent finite-size effects having no analogs in an infinite plane. Most intriguing are the trajectories depicted in the middle panel of figure 1, propagating in *both* directions along the interface. Formally, this is possible since the total current, considered as a quadratic form, is neither positively nor negatively defined, and thus a generic quantum state composed of eigenstates with different n-s may also carry the current in opposite direction then each of the components.

In real sample of a finite size, edge states associated with a p–n junction derived in this appendix are always accompanied by edge states close to a physical system boundary transporting the charge in opposite direction, see figure B3(a). When a disk-shaped sample is clamped with circular electrodes, forming the Corbino setup, edge currents are eliminated by the outer lead and the schematic current distribution for the lowest modes, visualized in figure B3(b), may be closely reproduced by the physical current density (see figure 6(a) in the main text). Remarkably, the familiar Fleming's left hand rule, relating the directions of the current, the magnetic field,

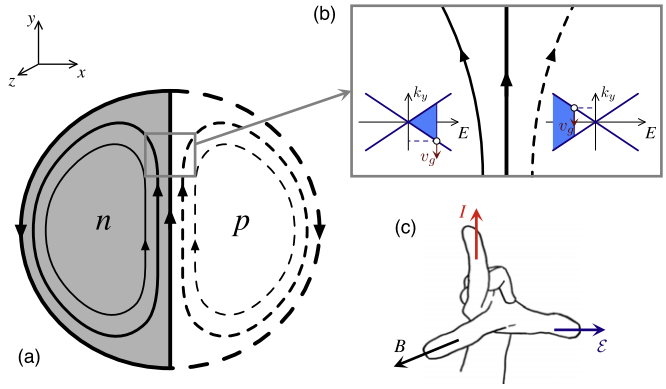

Figure B3. (a) Edge states in a finite disk-shaped graphene sample with a p–n interface in the quantum Hall regime (schematic). (b) A zoom-in of the interface region with band structure schemes. Open circles mark the two states on the Fermi level with opposite wavenumbers ($k_y < 0$ and $k_y > 0$) having equal group velocities (v_g). (Notice that the direction electric current is *opposite* to v_g as the electron charge is $-e$.) (c) A version of the Fleming's left hand rule showing mutual relation between directions of the magnetic field B, the in-plane electric field $\mathcal{E}$, and the current I near the interface. The coordinate system used in appendix B is also shown.

and the charge displacement (or the in-plane electric field) has also a version for graphene p–n junction in the quantum Hall regime, see figure B3(c).

Appendix C. Mass confinement and the valley separation

We argue here that the mechanism behind spatial separation of currents in different valleys, appearing for a nonzero mass term (see figure 6(b) in the main text), can essentially be understood by analyzing the zero-energy wavefunction in the presence of infinite mass confinement proposed in the seminal work by Berry and Mondragon [61].

In the absence of electric field ($\mathcal{E} = 0$), a general zero-energy solution of equation (B3) for $\xi = 1$ (the K valley) can be written as [62]

$$\Phi^{[\mathcal{E}=0]}_{0,k_y,\xi=1}(x) = C_1\begin{bmatrix}0\\ e^{-\chi^2/2}\end{bmatrix} + C_2\begin{bmatrix}e^{\chi^2/2}\\ 0\end{bmatrix}, \tag{C1}$$

with C_1 and C_2 being arbitrary complex numbers, and $\chi = l_B^{-1}x + l_B k_y$ again. For $\xi = -1$ (the K' valley), the two basis solutions on the right-hand side of equation (C1) have interchanged spinor components.

Neglecting the intervalley scattering, one can show that confinement of the carriers in a bounded domain implies zero outward current at any point of the boundary at each valley ($\xi = \pm 1$), namely

$$j_{\mathbf{n}(\alpha)} = \langle \xi\sigma_x \cos\alpha + \sigma_y \sin\alpha\rangle_{\Phi_\xi} = 0, \tag{C2}$$

where $\mathbf{n}(\alpha) = (\cos\alpha,\ \sin\alpha)$ is the unit vector normal to the boundary, and the spinor wavefunction $\Phi_\xi = (\Phi_{\xi,A},\ \Phi_{\xi,B})^T$. Equation (C2) can be rewritten as

$$\xi\cos\alpha\ \mathrm{Re}(\Phi^\star_{\xi,A}\Phi_{\xi,B}) + \sin\alpha\ \mathrm{Im}(\Phi^\star_{\xi,A}\Phi_{\xi,B}) = 0, \tag{C3}$$

which is equivalent to

$$\left(\frac{\Phi_{\xi,B}}{\Phi_{\xi,A}}\right)^\xi = i\mathcal{B}\exp(i\alpha), \tag{C4}$$

where $\mathcal{B}$ is real and depends on the physical nature of the confinement [61].

Infinite mass confinement at $x = 0$, restricting the wavefunction to the right hemiplane ($x > 0$), corresponds to $\mathcal{B} = 1$ and $\alpha = \pi$ in equation (C4) and leads to the boundary condition

$$\Phi_{\xi,A}|_{x=0} = i\xi\Phi_{\xi,B}|_{x=0}. \tag{C5}$$

Subsequently, the coefficients in equation (C1) follow

$$C_{\xi,2} = i\xi C_{\xi,1}\exp(-k_y^2 l_B^2). \tag{C6}$$

The vertical current density for the zero-energy solution is

$$j_y = \langle\sigma_y\rangle_{\Phi^{[\mathcal{E}=0]}_{0,k_y,\xi}} = -2\xi|C_{\xi,1}|^2\exp(-k_y^2 l_B^2), \tag{C7}$$

where the last equality follows from equation (C6).

Clearly, the uniform current in equation (C7) changes sign upon the valley exchange ($\xi \to -\xi$), providing a qualitative understanding of the valley separation, as the effect associated with zero-energy mode should overrule the effects originating from higher modes for a generic system close to the charge-neutrality point (allowing for $|k_y l_B| \ll 1$).

ORCID iDs

Adam Rycerz https://orcid.org/0000-0001-7873-0183

References

[1] Banerjee M, Heiblum M, Umansky V, Feldman D E, Oreg Y and Stern A 2018 Observation of half-integer thermal Hall conductance *Nature* **559** 205
[2] Mross D F, Oreg Y, Stern A, Margalit G and Heiblum M 2018 Theory of disorder-induced half-integer thermal hall conductance *Phys. Rev. Lett.* **121** 026801
[3] Beenakker C W J, Emary C, Kindermann M and van Velsen J L 2003 Proposal for production and detection of entangled electron-hole pairs in a degenerate electron gas *Phys. Rev. Lett.* **91** 147901
[4] Williams J R, Dicarlo L and Marcus C M 2007 Quantum hall effect in a gate-controlled p–n junction of graphene *Science* **317** 638
[5] Abanin D A and Levitov L S 2007 Quantized transport in graphene p–n junctions in a magnetic field *Science* **317** 641
[6] Carmier P, Lewenkopf C and Ullmo D 2011 Semiclassical magnetotransport in graphene n-p junctions *Phys. Rev.* B **84** 195428
[7] Zimmermann K, Jordan A, Gay F, Watanabe K, Taniguchi T, Han Z, Bouchiat V, Sellier H and Sacépéa B 2017 Tunable transmission of quantum Hall edge channels with full degeneracy lifting in split-gated graphene devices *Nat. Commun.* **8** 14983
[8] Qi C, Ouyang L and Hu J 2018 Realizing robust large-gap quantum spin Hall state in 2D HgTe monolayer on insulating substrate *2D Mater* **5** 045012
[9] Fujita M, Wakabayashi K, Nakada K and Kusakabe K 1996 Peculiar localized state at zigzag graphite edge *J. Phys. Soc. Japan* **65** 1920
[10] Nakada K, Fujita M, Dresselhaus G and Dresselhaus M S 1996 Edge state in graphene ribbons: nanometer size effect and edge shape dependence *Phys. Rev.* B **54** 1795
[11] Colomés E and Franz M 2018 Antichiral edge states in a modified Haldane nanoribbon *Phys. Rev. Lett.* **120** 086603
[12] Schaibley J R, Yu H, Clark G, Rivera P, Ross J S, Seyler K L, Yao W and Xu X 2016 Valleytronics in 2D materials *Nat. Rev. Mater.* **1** 16055
[13] Rycerz A, Tworzydło J and Beenakker C W J 2007 Valley filter and valley valve in graphene *Nat. Phys.* **3** 172
[14] Rycerz A 2008 Nonequilibrium valley polarization in graphene nanoconstrictions *Phys. Status Solidi* a **205** 1281
[15] Gunlycke D and White C T 2011 Graphene valley filter using a line defect *Phys. Rev. Lett.* **106** 136806
[16] Akhmerov A R, Bardarson J H, Rycerz A and Beenakker C W J 2008 Theory of the valley-valve effect in graphene nanoribbons *Phys. Rev.* B **77** 205416
[17] Wimmer M, Adagideli I, Berber S, Tománek D and Richter K 2008 Spin currents in rough graphene nanoribbons: universal fluctuations and spin injection *Phys. Rev. Lett.* **100** 177207
[18] Zhai F, Ma Y and Zhang Y-T 2011 A valley-filtering switch based on strained graphene *J. Phys.: Condens. Matter.* **23** 385302
[19] Jiang Y, Low T, Chang K, Katsnelson M I and Guinea F 2013 Generation of pure bulk valley current in graphene *Phys. Rev. Lett.* **110** 046601
[20] Settnes M, Power S R, Brandbyge M and Jauho A-P 2016 Graphene nanobubbles as valley filters and beam splitters *Phys. Rev. Lett.* **117** 276801
[21] Milovanović S P and Peeters F M 2016 Strain controlled valley filtering in multi-terminal graphene structures *Appl. Phys. Lett.* **109** 203108
[22] Zhang X-P, Huang C and Cazalilla M A 2017 Valley Hall effect and nonlocal transport in strained graphene *2D Mater.* **4** 024007
[23] Zhang Y, Guo B, Zhai F and Jiang W 2018 Valley-polarized edge pseudomagnetoplasmons in graphene: a two-component hydrodynamic model *Phys. Rev.* B **97** 115455
[24] Pályi A and Burkard G 2011 Disorder-mediated electron valley resonance in carbon nanotube quantum dots *Phys. Rev. Lett.* **106** 086801
[25] Schroer A, Silvestrov P G and Recher P 2015 Valley-based Cooper pair splitting via topologically confined channels in bilayer graphene *Phys. Rev.* B **92** 241404(R)
[26] Cheng S-G, Liu H, Jiang H, Sun Q-F and Xie X C 2018 Manipulation and characterization of the valley-polarized topological kink states in graphene-based interferometers *Phys. Rev. Lett.* **121** 156801
[27] Pan H, Li X, Zhang F and Yang S A 2015 Perfect valley filter in a topological domain wall *Phys. Rev.* B **92** 041404(R)
[28] Gorbachev R *et al* 2014 Detecting topological currents in graphene superlattices *Science* **346** 448
[29] Mak K F, McGill K L, Park J and McEuen P L 2014 The valley Hall effect in MoS_2 transistors *Science* **344** 1489
[30] Shimazaki Y, Yamamoto M, Borzenets I V, Watanabe K, Taniguchi T and Tarucha S 2015 Generation and detection of pure valley current by electrically induced Berry curvature in bilayer graphene *Nat. Phys.* **11** 1032
[31] Rickhaus P, Makk P, Liu M-H, Tóvári E, Weiss M, Maurand R, Richter K and Schönenberger C 2015 Snake trajectories in ultraclean graphene p–n junctions *Nat. Commun.* **6** 6470
[32] Makk P, Handschin C, Tovari E, Watanabe K, Taniguchi T, Richter K, Liu M-H and Schonenberger C 2018 Coexistence of classical snake states and Aharonov–Bohm oscillations along graphene p–n junctions *Phys. Rev.* B **98** 035413
[33] Liu Y, Tiwari R P, Brada M, Bruder C, Kusmartsev F V and Mele E J 2015 Snake states and their symmetries in graphene *Phys. Rev.* B **92** 235438
[34] Rycerz A 2010 Magneto conductance of the Corbino disk in graphene *Phys. Rev.* B **81** 121404(R)
[35] Katsnelson M I 2010 Aharonov–Bohm effect in undoped graphene: magnetotransport via evanescent waves *Europhys. Lett.* **89** 17001
[36] Peters E C, Giesbers A J M, Burghard M and Kern K 2014 Scaling in the quantum Hall regime of graphene Corbino devices *Appl. Phys. Lett.* **104** 203109
[37] Kumar M, Laitinen A and Hakonen P 2018 Unconventional fractional quantum Hall states and Wigner crystallization in suspended Corbino graphene *Nature Commun.* **9** 2776
[38] Katsnelson M I 2012 *Graphene: Carbon in Two Dimensions* (Cambridge: Cambridge University Press) ch 1

[39] Boukhvalov D W and Katsnelson M I 2009 Chemical functionalization of graphene *J. Phys.: Condens. Matter* **21** 344205
[40] Haberer D *et al* 2010 Tunable band gap in hydrogenated quasi-free-standing graphene *Nano Lett.* **10** 3360
[41] Hong J, Bekyarova E, de Heer W A, Haddon R C and Khizroev S 2013 Chemically engineered graphene-based 2D organic molecular magnet *ACS Nano* **7** 10011
[42] Sachs B, Wehling T O, Katsnelson M I and Lichtenstein A I 2011 Adhesion and electronic structure of graphene on hexagonal boron nitride substrates *Phys. Rev.* B **84** 195444
[43] Yankowitz M, Xue J and LeRoy B J 2014 Graphene on hexagonal boron nitride *J. Phys.: Condens. Matter* **26** 303201
[44] Rycerz A 2013 Strain-induced transitions to quantum chaos and effective time-reversal symmetry breaking in triangular graphene nanoflakes *Phys. Rev.* B **87** 195431
[45] Rut G and Rycerz A 2016 Trigonal warping, pseudodiffusive transport, and finite-system version of the Lifshitz transition in magnetoconductance of bilayer graphene Corbino disks *Phys. Rev.* B **93** 075419
[46] Landauer R 1970 Electrical resistance of disordered one-dimensional lattices *Phil. Mag.* **21** 863
[47] Büttiker M 1992 Scattering theory of current and intensity noise correlations in conductors and wave guides *Phys. Rev.* B **46** 12485
[48] Müller M, Schmalian J and Fritz L 2009 Graphene: a nearly perfect fluid *Phys. Rev. Lett.* **103** 025301
[49] Lucas A and Fong K C 2018 Hydrodynamics of electrons in graphene *J. Phys.: Condens. Matter* **30** 053001
[50] Lukose V, Shankar R and Baskaran G 2007 Novel electric field effects on landau levels in graphene *Phys. Rev. Lett.* **98** 116802
[51] Shytov A, Rudner M, Gu N, Katsnelson M and Levitov L 2009 Atomic collapse, Lorentz boosts, Klein scattering, and other quantum-relativistic phenomena in graphene *Sol. State Commun.* **149** 1087
[52] Beenakker C W J 2008 Andreev reflection and Klein tunneling in graphene *Rev. Mod. Phys.* **80** 1337
[53] Wimmer M 2009 Quantum transport in nanostructures: from computational concepts to spintronics in graphene and magnetic tunnel junctions *PhD Thesis* Regensburg University, Germany ch 6
[54] Bardarson J H, Tworzydło J, Brouwer P W and Beenakker C W J 2007 Demonstration of one-parameter scaling at the Dirac point in graphene *Phys. Rev. Lett.* **99** 106801
[55] Rycerz A 2012 Random matrices and quantum chaos in weakly-disordered graphene nanoflakes *Phys. Rev.* B **85** 245424
[56] Burden R L and Faires J D 2011 *Numerical Analysis* (Boston: Brooks/Cole) ch 5
[57] Peres N M R and Castro E V 2007 Algebraic solution of a graphene layer in transverse electric and perpendicular magnetic fields *J. Phys.: Condens. Matter* **19** 406231
[58] Nath D and Roy P 2014 Dirac oscillator in perpendicular magnetic and transverse electric fields *Ann. Phys.* **351** 13
[59] Abramowitz M and Stegun I A (ed) 1965 *Handbook of Mathematical Functions* (New York: Dover Publications) ch 19
[60] MacDonald A H 1983 Quantized Hall conductance in a relativistic two-dimensional electron gas *Phys. Rev.* B **28** 2235
[61] Berry M V and Mondragon R I 1987 Neutrino billiards: time-reversal symmetry-breaking without magnetic fields *Proc. R. Soc.* A **41** 53
[62] Prada E, San-Jose P, Wunsch B and Guinea F 2007 Pseudo-diffusive magnetotransport in graphene *Phys. Rev.* B **75** 113407